CrystEngComm

ROYAL SOCIETY
OF **CHEMISTRY**

PAPER
Duane Choquesillo-Lazarte *et al.*
Evaluation of synthon influence on ethenzamide–polyphenol
pharmaceutical cocrystals

PAPER

Check for updates

Evaluation of synthon influence on ethenzamide–polyphenol pharmaceutical cocrystals†

Francisco Javier Acebedo-Martínez, [iD] [a] Alicia Domínguez-Martín, [iD] [b] Carolina Alarcón-Payer, [iD] [c] Antonio Frontera, [iD] [d] Ángel Ibáñez[b] and Duane Choquesillo-Lazarte [iD] *[a]

The pharmaceutical cocrystal landscape of ethenzamide has been addressed during the past years with the aim of improving its physicochemical properties, mainly solubility and dissolution rate. Herein four novel ethenzamide cocrystals have been isolated by mechanochemical synthesis and thoroughly characterized by powder and single-crystal X-ray diffraction. Polyphenols have been selected as coformers based on ethenzamide synthon preference as well as their safety profile and antioxidant character. Besides crystallographic analysis, theoretical calculations have been made to evaluate the strength of intermolecular interactions and their role in crystal packing. The results evidence differences in the supramolecular architecture depending on the different polyphenolic isomers used as coformers. Finally, the physicochemical properties of the novel compounds were assessed and compared to those of ethenzamide alone. Although the solubility profile is significantly enhanced, the thermodynamic stability of the novel cocrystals in aqueous medium is restricted to 24 hours. These findings have been correlated with the crystal structure.
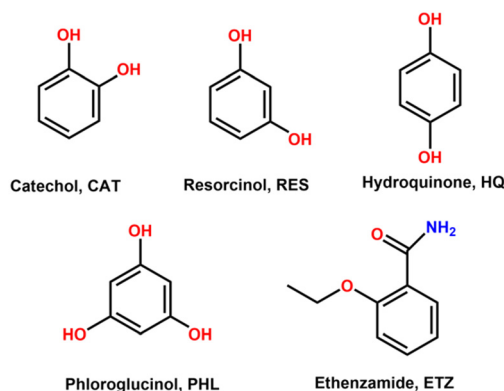
Introduction

Ethenzamide (ETZ, Scheme 1) is defined as a non-steroidal anti-inflammatory drug (NSAID), which has been proved to have analgesic, antipyretic, anti-inflammatory, and antirheumatic properties. Its detailed mechanism of action still remains uncertain, yet ETZ is widely used in clinics, sometimes in combination with other NSAIDs.[1–3] ETZ belongs to class II drugs in the Biopharmaceutical Classification System (BSC), *i.e.*, it shows a rather poor solubility in water (0.034 mg mL^{-1}) as well as poor permeation through biological membranes,[4] thus compromising its oral bioavailability. Consequently, a wide number of references can be found regarding strategies either to enhance its solubility or to improve its dissolution rate. Prior studies

sought carriers for this purpose;[5–7] however, more recent studies focus their attention on crystal engineering strategies such as the design of multicomponent pharmaceutical solids.[8,9]

Multicomponent pharmaceutical solids such as pharmaceutical cocrystals require at least one active pharmaceutical ingredient (API) and a coformer. Coformers can be another API, as observed in fixed-dose combinations, or other molecules regarded as safe, usually considered among those included in the U.S. Food and Drug Administration (FDA) lists 'Substances Added to Food' and/

[a] *Laboratorio de Estudios Cristalográficos, IACT, CSIC-Universidad de Granada, Avda. de las Palmeras 4, 18100 Armilla, Spain. E-mail: duane.choquesillo@csic.es*
[b] *Department of Inorganic Chemistry, Faculty of Pharmacy, University of Granada, 18071 Granada, Spain*
[c] *Servicio de Farmacia, Hospital Universitario Virgen de las Nieves, 18014 Granada, Spain*
[d] *Department of Chemistry, Universitat de les Illes Balears, Crta de Valldemossa km 7.5, 07122 Palma de Mallorca, Baleares, Spain*

† Electronic supplementary information (ESI) available: PXRD, DSC/TG data for the studied cocrystals. CCDC 2247944–2247947. For ESI and crystallographic data in CIF or other electronic format see DOI: https://doi.org/10.1039/d3ce00234a

Scheme 1 Chemical formula of catechol (CAT), resorcinol (RES), hydroquinone (HQ), phloroglucinol (PHL), and ethenzamide (ETZ).

or 'Generally Recognized As Safe' (GRAS).[10,11] To date, several ETZ cocrystal can be found in the literature,[12–15] including the characterization of cocrystal polymorphs.[4,16–18]

It is claimed that NSAIDs, such as ETZ, can exert antioxidant properties, working as free radical scavengers.[19] However, in such cases, the anti-inflammatory effect of NSAIDs might be reduced. Therefore, some authors have explored the possibility of formulating ETZ with antioxidant molecules to improve its efficacy.[20] In this context, polyphenols can be considered as good candidate coformers, since they are known for their strong antioxidant power and their safety profile. Indeed, polyphenols have been widely used by the pharmaceutical and nutraceutical industries[21–23] and have recently been used in multicomponent solid formulations.[24–27]

The aim of this work is to synthesize and characterize novel ETZ–polyphenol cocrystals. Herein, polyphenol isomers (catechol, resorcinol, hydroquinone, Scheme 1) and phloroglucinol (Scheme 1) have been used as coformers, taking advantage of the versatile role that the hydroxyl groups present in polyphenols play in the construction of supramolecular networks. It should be noted that the polyphenol hydroquinone is authorized only for topical use and at very low doses due to the reported concerns about possible carcinogenicity and a link to ochronosis; thereby it is currently not included in the 'Generally Recognized as Safe and Effective' (GRASE) list from the U.S. FDA. Nonetheless, the goal of this study is not only to propose suitable industrial candidates but also to evaluate how the relative position of the –OH groups in the polyphenol coformers affects the crystal architecture and rationalize such results in terms of structure–property relationships. To achieve this purpose, a thorough crystallographic and theoretical study has been carried out, including an energetic analysis of the present intermolecular interactions, mainly H-bonding and π–π stacking. Moreover, the physicochemical properties of the novel cocrystals have also been studied, including their thermal and thermodynamic stability in aqueous medium and solubility. Finally, a rational structure–property analysis of the novel multicomponent solids has been performed.

Results and discussion

Coformer selection

To improve the success rate of the experiments, we conducted a virtual cocrystal screening prior to the execution of the trials. A survey of the Cambridge Structural Database[28] (CSD version 5.43, update 4 from Nov 2022) using ETZ as the target molecule resulted in 52 hits. After excluding hits with only ETZ molecules, we were left with 49 hits, which corresponded to multicomponent crystals, including cocrystals[4,12,14–16,18,29–37] and solvates.[17,38–41] A robust $R_2^2(8)$ amide–amide homosynthon was observed in the crystal structure of ETZ.[32,42] The ETZ amide group plays a critical role in the interaction with the coformer. Hence, the abundance of heterosynthons observed in the survey followed the order amide–carboxylic (51%) > amide–amide

(20%) > amide–hydroxyl (phenol) (10%) > amide–carbonyl (6%). These results also show that in some multicomponent crystalline phases, ETZ preserves its dimeric structure[12,35,36,41] or forms infinite $C_1^1(4)$ ETZ chains[12,33,39] (Scheme 2).

Based on these results, the use of polyphenolic molecules as coformers in this study is in good agreement with the observed synthon preference in reported structures containing ETZ. To validate our selection, we used the COSMOQuick[43] software to predict the tendency of cocrystal formation based on thermodynamic calculations. This tool calculates the excess enthalpy of formation (H_{ex}) between ETZ and the corresponding coformer relative to the pure components in the supercooled liquid phase.[44] The list of candidates for the formation of multicomponent crystals with ETZ, including our polyphenolic molecules and other coformer molecules involved in the formation of cocrystals reported in the survey, was analyzed. Compounds with negative H_{ex} values have an increased probability of forming cocrystals because H_{ex} is a rough approximation of the free energy of cocrystal formation, $\Delta G_{cocrystal}$. Fig. 1 presents the results obtained from the systems examined in this study, which can serve as a qualitative indicator for the likelihood of cocrystal formation and confirm the preference of ETZ for forming cocrystals with coformers that exhibit the functional groups observed in the CSD survey, including our coformer candidates.

Mechanochemical synthesis

Liquid-assisted grinding (LAG) is a mechanochemical synthesis technique that is widely used for the screening and synthesis of new multicomponent materials because of its low time and resource consumption.[45] In this work, four new cocrystals of ETZ were obtained by LAG, where a 2:1 stoichiometric mixture of ETZ and the respective coformer was placed in a stainless-steel jar with two stainless-steel balls and 100 μL of liquid additive. A comparison of the PXRD patterns of the reaction products with those of the parent components indicated the formation of new cocrystals (Fig. S1†).

Prior to the obtention of the cocrystals and during the screening process, neat grinding of mixtures of ETZ with the respective coformers in 1:1, 1:2, and 2:1 stoichiometries
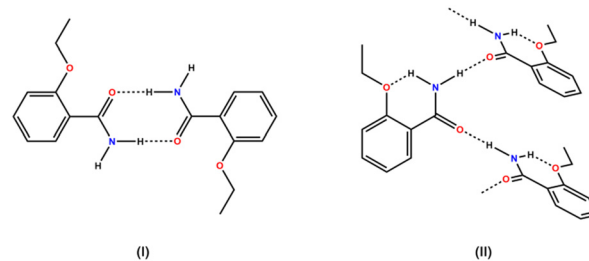
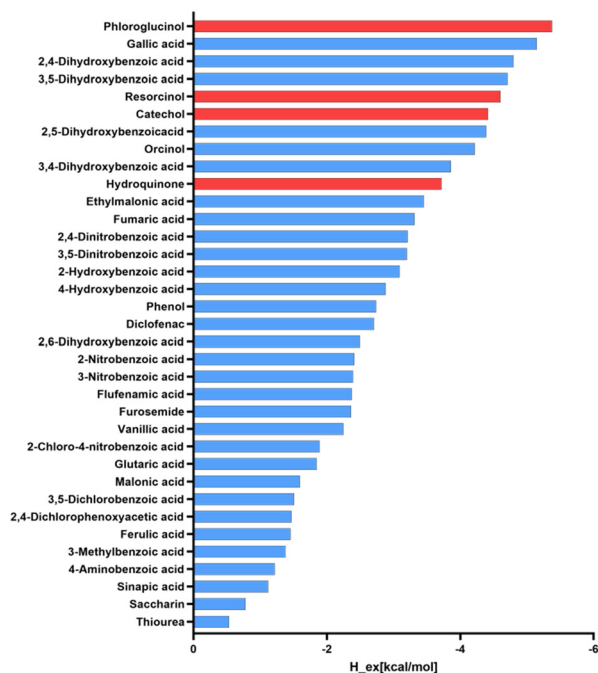Scheme 2 Supramolecular ETZ association in reported ETZ cocrystals: (I) ETZ dimer and (II) ETZ infinite chain.

Fig. 1 Ranking positions for ETZ coformers reported in the CSD (blue) including the polyphenolic molecules used in this study (red) based on COSMOQuick calculations.

Fig. 2 Powder X-ray diffraction (PXRD) patterns of ETZ and the pure cocrystals obtained by liquid-assisted grinding (LAG).

heterosynthon. In the crystal, a centrosymmetric $R_2^2(8)$ amide : amide homosynthon is observed, similar to the reported ethenzamide parent structure. CAT adopts an *anti–anti*

was performed, leading to the formation of physical mixtures. Only a 2 : 1 stoichiometric ratio resulted in the formation of new materials, but with a very low performance ratio. Fig. S2† shows the PXRD patterns of the new grindings with different stoichiometries for all the ETZ–coformer combinations. Liquid additives were used to induce the formation of the aforementioned new phases. LAG reactions with ethanol led to the formation of **ETZ–RES** and **ETZ–HQ** phases, whereas acetonitrile and hexane led to the formation of **ETZ–PHL** and **ETZ–CAT** (Fig. S3†).

To determine the crystalline structure of the new phases, single crystals of the materials were obtained by slow solvent evaporation of saturated solutions of the LAG product in several organic solvents such as ethanol and acetonitrile. After two days of evaporation at room temperature, crystals suitable for single-crystal X-ray diffraction (SCXRD) were obtained and carefully separated. Crystal structure determination also proved the purity of the bulk product obtained by LAG owing to the good agreement between the PXRD pattern of the product of the LAG and the PXRD pattern calculated from the crystalline structure, as shown in Fig. 2.

Structural analysis of ETZ cocrystals

ETZ–CAT cocrystal. **ETZ–CAT** crystallizes in the triclinic space group $P\bar{1}$ with two ETZ molecules (ETZ1 and ETZ2) and one CAT molecule in the asymmetric unit, resulting in a cocrystal with a 2 : 1 stoichiometric ratio (Fig. 3a), where CAT bridges two ETZ molecules through the phenol–amide
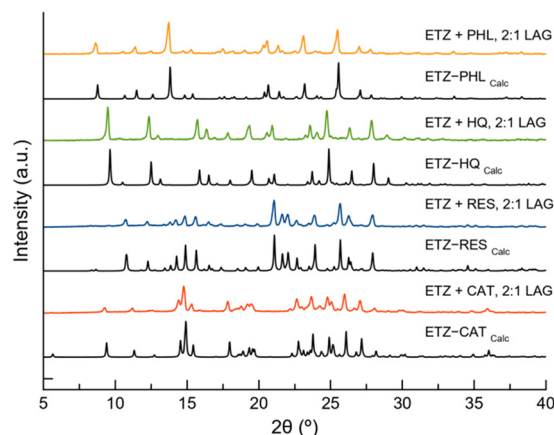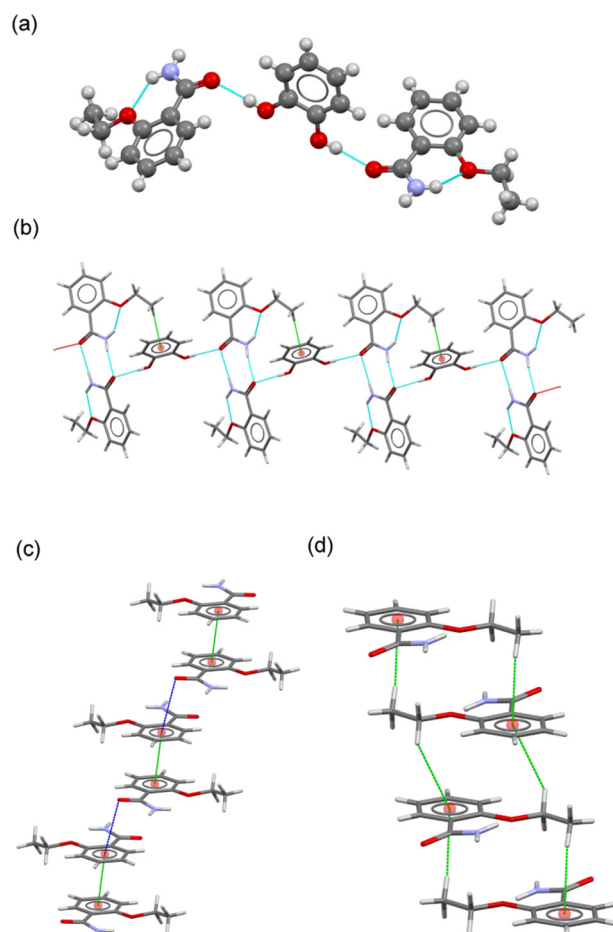

Fig. 3 (a) Asymmetric unit in the cocrystal **ETZ–CAT**. (b) Fragment of the ribbon structure in **ETZ–CAT**. (c) Details of the π–π stacking interactions between ETZ1 molecules. (d) Details of the C–H⋯π interactions between ETZ2 molecules.

conformation and associates with ETZ–ETZ dimers by H-bonding interactions, generating a ribbon-like structure reinforced by C–H⋯π interactions between the terminal methyl group of ETZ2 and the aromatic ring of CAT (Fig. 3b). The supramolecular structure of the crystal results from the additional participation of noncovalent interactions involving the ETZ1 and ETZ2 molecules, which associate with each other (Fig. 3c and d). On the one hand, pairs of ETZ1 molecules form a centrosymmetric dimer by π–π stacking interactions, which are further connected by C=O⋯π interactions, generating an infinite column. In contrast, ETZ2 molecules generate a centrosymmetric multi-stacked column *via* C–H⋯π interactions. Therefore, the 3D structure was obtained by connecting these columns through H-bonds and C–H⋯O interactions involving CAT coformers.

ETZ–RES cocrystal. The crystal structure of **ETZ–RES** was solved in the monoclinic space group $P2_1/c$, and the asymmetric unit consisted of two ETZ molecules (ETZ1 and ETZ2) and one RES molecule (Fig. 4a). The hydroxyl groups of the RES molecule adopt a *syn–anti* conformation and connect the ETZ molecules through phenol:amide discrete heterosynthons (graph set $D_1^1(2)$). Amide:amide ETZ dimers were also observed in the **ETZ–RES** cocrystal. They were connected by RES molecules, generating chain structures extending along the 2_1 screw axes (Fig. 4b). π–π stacking interactions between the aromatic rings of ETZ1 and ETZ2 molecules from different chains generated an interdigitated layer structure extending parallel to the *bc* plane (Fig. 4c). C–H⋯O interactions further associated the layers with the generation of the 3D structure.

ETZ–HQ cocrystal. **ETZ–HQ** crystallized in the triclinic space group $P\bar{1}$. The asymmetric unit consists of a molecule of ETZ and half a molecule of HQ located in an inversion center, leading to a 2 : 1 stoichiometric ratio, where each HQ molecule
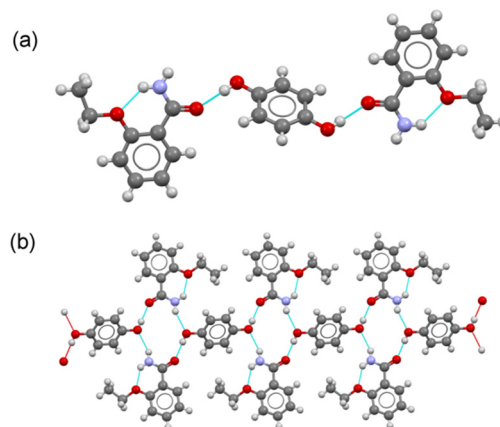
Fig. 5 (a) Asymmetric unit in the cocrystal **ETZ–HQ**. (b) Fragment of tape structure built by H-bonding interactions.

connects two ETZ molecules *via* a phenol–amide heterosynthon on each side (graph set $D_1^1(2)$) (Fig. 5a). Each ETZ : HQ : ETZ unit is further connected by an N–H(amide)⋯O(phenol) hydrogen bond to other units, resulting in a tape structure running along the *c*-axis (Fig. 5b). In the crystal structure, the robust $R_2^2(8)$ amide:amide homosynthon dimer was disrupted by the insertion of HQ molecules. The tape structures were then connected by C–H⋯O and amide⋯π interactions, generating a
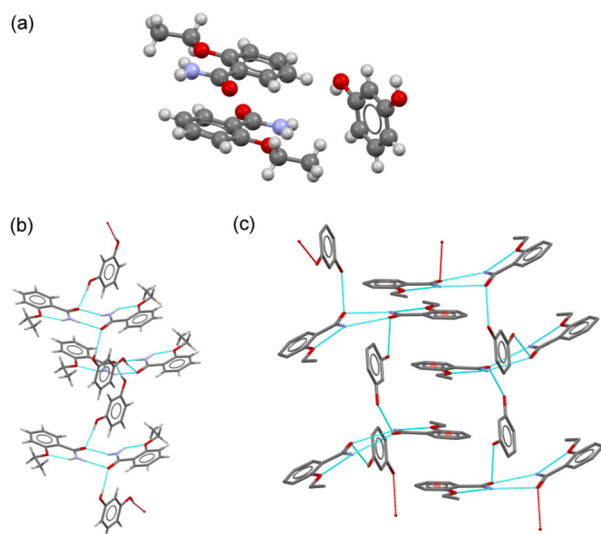
Fig. 4 (a) Asymmetric unit in the cocrystal **ETZ–RES**. (b) Detailed view of the chain structure in **ETZ–RES**. (c) Fragment of 2D layered structure generated by π–π stacking interactions.
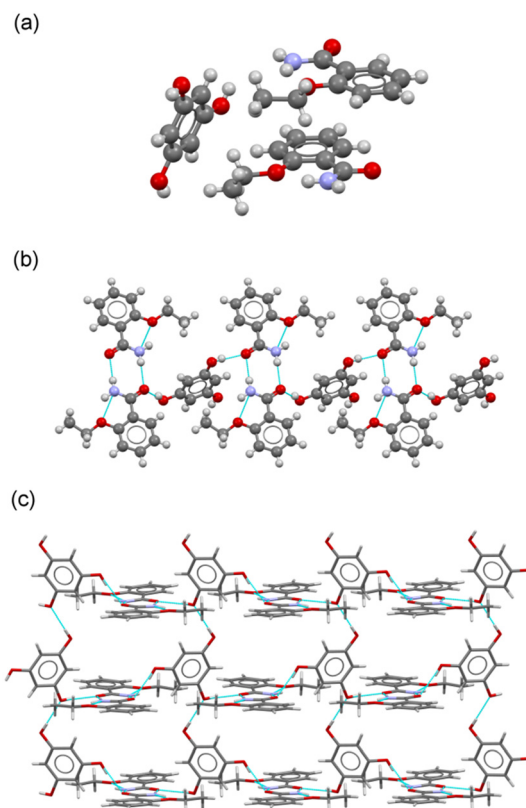
Fig. 6 (a) Asymmetric unit in the cocrystal **ETZ–PHL**. (b) Detailed view of the tape structure in **ETZ–PHL**. (c) Fragment of 2D grid structure in **ETZ–PHL**.

2D layer structure extending parallel to the *bc* plane. These layers are stacked along the *a*-axis, resulting in 3D crystal packing.

ETZ–PHL cocrystal. The **ETZ–PHL** cocrystal belongs to the monoclinic system with the *Pn* space group. The asymmetric unit of the cocrystal consisted of ETZ and PHL molecules in a 2 : 1 molar ratio (Fig. 6a). As in the case of the cocrystals with CAT and RES as coformers, a robust amide : amide dimer homosynthon was observed. PHL molecules then connect dimers through two of their –OH groups (positions 1 and 3), resembling a *syn–anti* RES coformer, generating a tape structure with ETZ : ETZ dimers located in the periphery (Fig. 6b). The third –OH of the PHL is used to connect adjacent PHL molecules by –OH⋯O H-bonding interactions, affording a 2D grid structure, as illustrated in Fig. 6c. These structures are then associated by π–π stacking interactions involving two crystallographically independent ETZ molecules to build an interdigitated 3D structure reinforced by N–H⋯O H-bonds.

Theoretical studies

The theoretical study is focused on the evaluation of H-bonding interactions as well as several π–π stacking complexation modes in ETZ cocrystals with polyphenolic coformers. One of our purposes is to analyze the formation of self-assembled ETZ dimers by means of two N–H⋯O bonds ($R_2^2(8)$ synthon) in **ETZ–CAT**, **ETZ–RES**, and **ETZ–PHL**, and the absence of such dimers in **ETZ–HQ** (see Scheme 3). As further commented below, in those co-crystals where the $R_2^2(8)$ self-assembled dimers are formed, the polyphenolic coformers connect the dimers through strong O–H⋯O H-bonds.

First, we have computed the molecular electrostatic potential (MEP) surfaces of all coformers, which are represented in Fig. 7. They evidence that ETZ is the best H-bond acceptor with the minimum MEP value located at the amidic O atoms (−48 kcal mol^{-1}). The MEP maximum is located at the amidic H atom (+32 kcal mol^{-1}). The MEP value over the aromatic ring is negative (−12 kcal mol^{-1}) and positive at the H atoms of the ethyl (+20 kcal mol^{-1}). The MEP value over the center of the aromatic ring in the rest of the coformers (polyphenols) is also negative, thus explaining
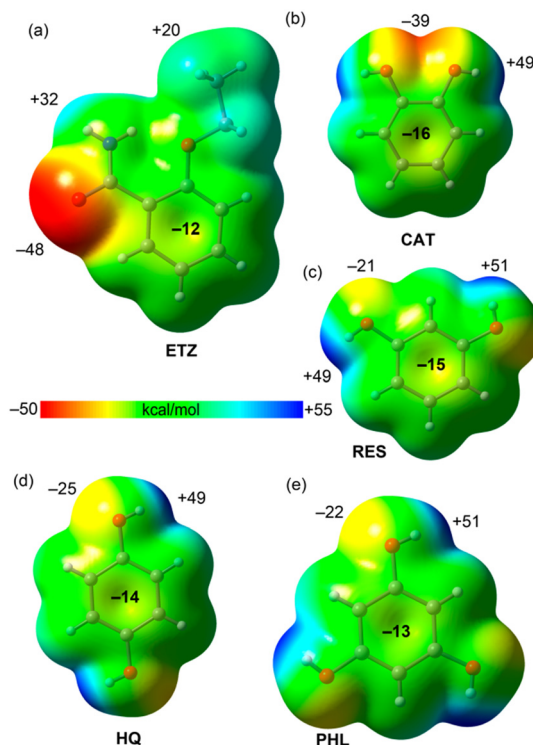

Fig. 7 MEP surfaces of ETZ (a), CAT (b), RES (c), HQ (d) and PHL (e) at the PBE0-D3/def2-TZVP. Isosurface 0.001 a.u. The MEP values at selected points of the surfaces are given in kcal mol^{-1}.

the formation of C–H⋯π interactions in the solid state of some of these compounds (*vide infra*).

The MEP surfaces of the polyphenols show that they are excellent H-bond donors, as expected, with values ranging from +48 to +51 kcal mol^{-1} at the phenolic H atoms. However, they are worse H-bond acceptors than ETZ, with MEP values ranging from −21 kcal mol^{-1} to −39 kcal mol^{-1}. The best H-bond acceptor is CAT due to the overlap of two lone pairs. For latter compounds, we have used the conformation observed in the solid state, which are not the global minima.

Several π–π stacking modes of the ETZ molecule (homodimers) exist in the solid state of the cocrystals, which are represented in Fig. 8 and 9, along with their QTAIM and NCIPlot analyses. Interestingly, in three of them the fused H-bonded ring also participates in the binding (**ETZ–RES**, **ETZ–HQ** and **ETZ–PHL**); see Fig. 8. In these complexes, the π-stacking is characterized by several bonds, green and cage critical points (CPs), represented by red, yellow and blue spheres. The bond CPs interconnect several atoms of both ETZ molecules, including those of the H-bonded six-membered ring (highlighted in fuchsia). It is interesting to highlight that in the case of **ETZ–RES** the antiparallel stacking is an almost perfect face-to-face stacking where the H-bonded ring is precisely located over the aromatic ring and *vice versa*.

The existence of π–π stacking interactions is further confirmed by the NCIPlot index analysis that shows a green
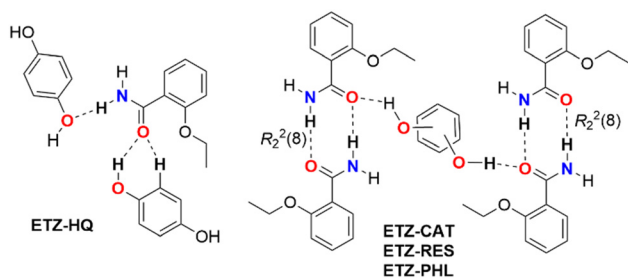
Scheme 3 Different H-bonding networks in the cocrystals reported herein.
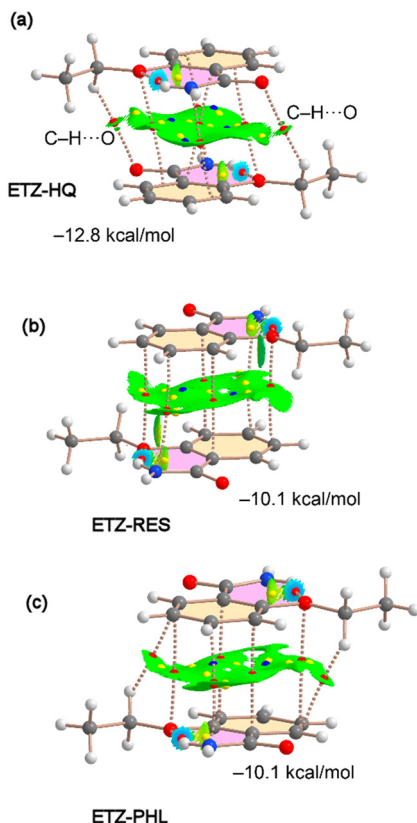
Fig. 8 Distribution of bond, ring and cage critical points (red, yellow and blue spheres, respectively) and bond paths in the π-stacking dimers of **ETZ–HQ** (a), **ETZ–RES** (b) and **ETZ–PHL** (c). The overlapped NCIPlot index analysis is also shown. RDG isosurface 0.5 a.u., density cutoff = 0.04 a.u., color range: −0.04 a.u.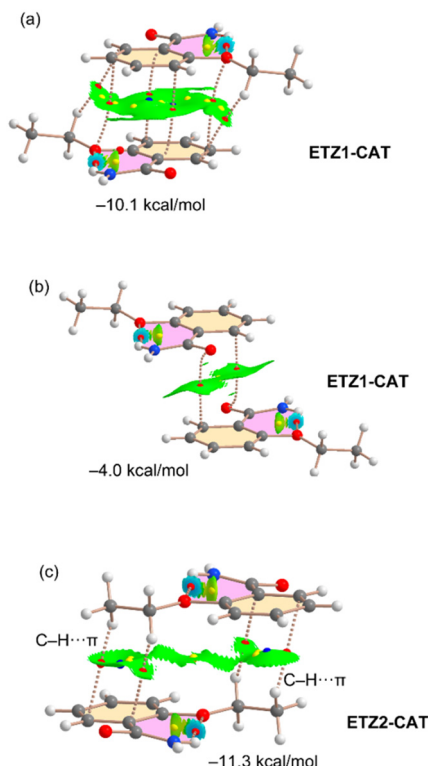 ≤ sign(λ_2) × ρ ≤ 0.04 a.u. Only the noncovalent interactions are represented in both QTAIM and NCIPlot analyses.

Fig. 9 Distribution of bond, ring and cage critical points (red, yellow and blue spheres, respectively) and bond paths in the π-stacking dimers of ETZ1–CAT (a and b) and ETZ2–CAT (c). The overlapped NCIPlot index analysis is also shown. RDG isosurface 0.5 a.u., density cutoff = 0.04 a.u., color range: −0.04 a.u. ≤ sign(λ_2) × ρ ≤ 0.04 a.u. Only the noncovalent interactions are represented in both QTAIM and NCIPlot analyses.

isosurface (meaning attractive interaction) between the aromatic rings. We have computed the dimerization energies for the three homodimers and they are quite large, −12.8 kcal mol^{-1} for **ETZ–HQ** and −10.1 kcal mol^{-1} for **ETZ–RES** and **ETZ–PHL** cocrystals. The interaction energy is larger in **ETZ–HQ** likely due to the formation of two ancillary C–H⋯O interactions (see Fig. 8a) involving the ethyl group and the amidic O atom. This interaction is characterized by the corresponding bond CP, bond path and NCIPlot isosurface connecting the O and H atoms.

In the case of **ETZ–CAT** (Fig. 9), there are two symmetrically independent ETZ molecules in the X-ray structure, namely ETZ1 (ring C1–C6) and ETZ2 (ring C11–C16). We have found three different stacking modes, two involving ETZ1 and one involving ETZ2. One is similar to the bonding modes described in Fig. 8 with an antiparallel arrangement of the rings and identical binding energy (−10.1 kcal mol^{-1}, see Fig. 9a) compared to **ETZ–PHL** and **ETZ–RES**. In the other π–π stacking involving ETZ1, both π systems are significantly displaced and the interaction is characterized by two bond CPs that interconnect the carbonyl O atoms to the aromatic carbon atoms. This biding mode is energetically

weaker (−4.0 kcal mol^{-1}) likely due to the smaller overlap of the π systems, as corroborated by the NCIPlot isosurfaces.

Finally, the stacking mode observed for the ETZ2 moiety is characterized by the interaction of the ethyl groups with the aromatic rings, thus establishing two sets of symmetrically equivalent CH⋯π interactions that are characterized by two bond CPs and a bond path connecting two H atoms of the ethyl group to two carbon atoms of the aromatic rings (see Fig. 8c). Interestingly, this binding mode is slightly stronger than that of **ETZ1–CAT** (see Fig. 9a and b).

The combined QTAIM/NCIPlot analysis of the H-bonds observed in the solid state of cocrystal **ETZ–HQ** is shown in Fig. 10. In this compound, the self-assembled ETZ dimers were not formed. For this compound (and the rest of the compounds described below), each H-bond is characterized by a bond CP, a bond path and a green (weak) or blue (strong) NCIPlot isosurface, depending on the strength of the interaction. In fact, we have estimated the H-bond energy of the H-bonds using the potential energy density at the bond CP using the formula proposed by Espinosa *et al.*[46] (E_{dis} = 0.5 × V_r). The energies are summarized in Table 1. It can be observed that in the **ETZ–HQ** cocrystal the strongest H-bond is O–H⋯O (−8.25 kcal mol^{-1}), in agreement with the MEP analysis. The N–H⋯O is significantly weaker (−2.85 kcal

Fig. 10 Distribution of bond and ring critical points (red and yellow spheres, respectively) and bond paths in the H-bonding networks of **ETZ–HQ**. The overlapped NCIPlot index analysis is also shown. RDG isosurface 0.5 a.u., density cutoff = 0.04 a.u., color range: −0.04 a.u. ≤ sign(λ_2) × ρ ≤ 0.04 a.u. For clarity, only the noncovalent interactions are represented in both QTAIM and NCIPlot analyses.
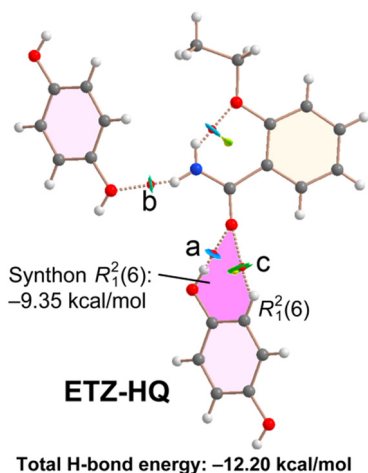
Table 1 QTAIM parameters at the bond CP (ρ, V_r, a.u.) and the dissociation energies (E_{dis}, kcal mol^{-1}) for the CP labelled in Fig. 10

Compound and CP	ρ	V_r	E_{dis}
ETZ–HQ (a)	0.0280	−0.0263	8.25
ETZ–HQ (b)	0.0140	−0.0091	2.85
ETZ–HQ (c)	0.0057	−0.0035	1.10

mol^{-1}), in line with the poor H-bond acceptor ability of the –OH. Finally, the dissociation energy of the C–H···O contact is only −1.10 kcal mol^{-1}. The energy associated to the $R_1^2(6)$ synthon (highlighted in pink) is significant (−9.35 kcal mol^{-1}), even larger than that of the $R_2^2(8)$ synthons observed in the rest of the cocrystals (*vide infra*).

Fig. 11 shows the QTAIM/NCIPlot combined analyses of cocrystals **ETZ–CAT**, **ETZ–RES** and **ETZ–PHL**, which have in common the formation of the ETZ self-assembled dimers, which are interconnected by the bridging polyphenolic rings. The formation energies of the $R_2^2(8)$ self-assembled dimers (highlighted in orange) can be estimated by summing the dissociation energies associated to two bond CPs that characterize the HBs. The energies are gathered in Table 2 and the formation energies range from −6.43 kcal mol^{-1} in **ETZ–RES** to −8.10 kcal mol^{-1} in **ETZ–PHL**. The total H-bond energy in the **ETZ–CAT** and **ETZ–RES** assemblies are comparable (−28.18 kcal mol^{-1} and −25.76 kcal mol^{-1}, respectively).

In general, the O–H···O(ETZ) HBs are stronger than the N–H···O HBs, in agreement with the superior H-bond donor ability of the phenol groups compared to that of the –NH$_2$ group of ETZ. In compound **ETZ–PHL**, where the aromatic ring presents three OH groups (PHL), two of them are used to interconnect the self-assembled ETZ dimers and the third one forms an HB with an adjacent PHL molecule (see CP "d" in Fig. 11c). This

Fig. 11 Distribution of bond and ring critical points (red and yellow spheres, respectively) and bond paths for the H-bonding networks of **ETZ–CAT** (a), **ETZ–RES** (b) and **ETZ–PHL** (c). The overlapped NCIPlot index analysis is also shown. RDG isosurface 0.5 a.u., density cutoff = 0.04 a.u., color range: −0.04 a.u. ≤ sign(λ_2) × ρ ≤ 0.04 a.u. For clarity, only the noncovalent interactions are represented in both QTAIM and NCIPlot analyses.
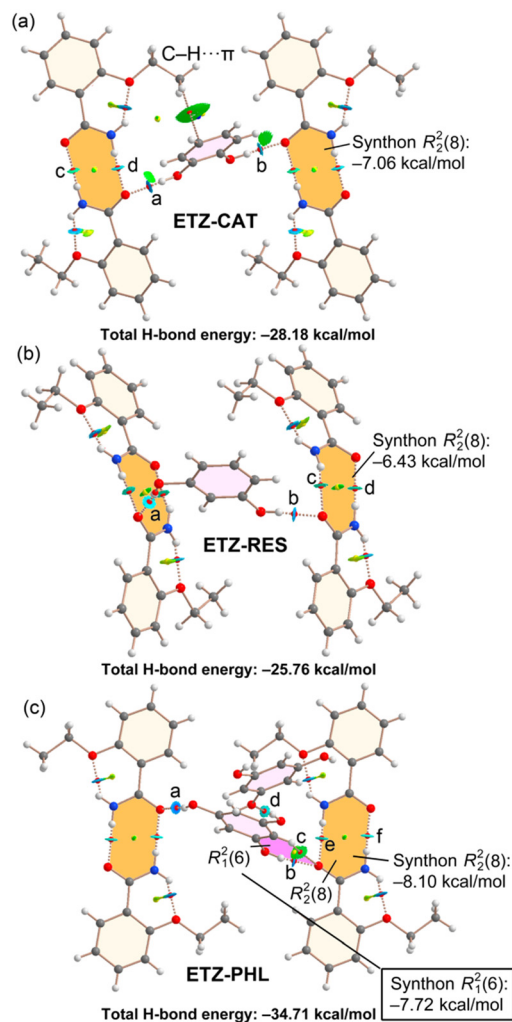
Table 2 QTAIM parameters at the bond CP (ρ, V_r, a.u.) and the dissociation energies (E_{dis}, kcal mol^{-1}) for the CP labelled in Fig. 11

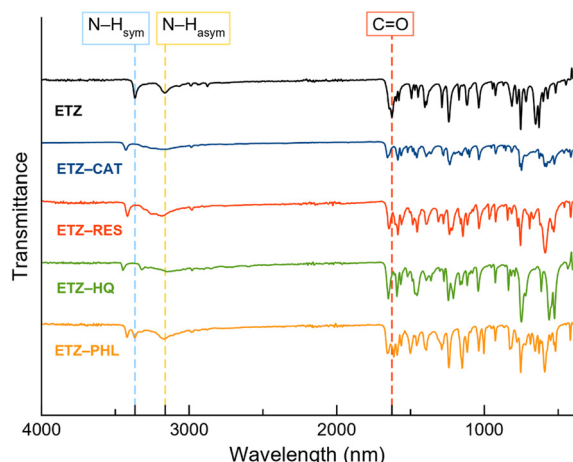| Compound and CP	ρ	V_r	E_{dis}
ETZ–CAT (a)	0.0264	−0.0240	7.53
ETZ–CAT (b)	0.0237	−0.0208	6.53
ETZ–CAT (c)	0.0127	−0.0035	1.10
ETZ–CAT (d)	0.0205	−0.0152	4.77
ETZ–RES (a)	0.0217	−0.0179	5.62
ETZ–RES (b)	0.0258	−0.0232	7.28
ETZ–RES (c)	0.0154	−0.0101	3.17
ETZ–RES (d)	0.0161	−0.0104	3.26
ETZ–PHL (a)	0.0280	−0.0260	6.46
ETZ–PHL (b)	0.0274	−0.0260	6.46
ETZ–PHL (c)	0.0066	−0.0040	1.26
ETZ–PHL (d)	0.0184	−0.0138	4.33
ETZ–PHL (e)	0.0185	−0.0129	4.05
ETZ–PHL (f)	0.0185	−0.0129	4.05

Fig. 12 FT-IR spectra of ETZ and the reported cocrystals.

OH···O(PHL) H-bond is weaker than the OH···O(ETZ) H-bonds, which range from −5.7 to −7.5 kcal mol^{-1}. In this assembly, the formation of a $R_1^2(6)$ synthon (highlighted in pink) is also observed, similar to that of the **ETZ–HQ** cocrystal (Fig. 10). The formation energy is also significant (−7.72 kcal mol^{-1}) but smaller than that of the **ETZ–HQ** cocrystal, likely due to the simultaneous participation of the amidic O atom in ETZ in the $R_2^2(8)$ synthon.

The combined QTAIM/NCIPlot analysis of **ETZ–CAT** (Fig. 11a) also evidences the formation of a C–H···π interaction that is characterized by a bond CP and a bond path connecting one H atom of the ethyl group with the aromatic ring of CAT. This is also confirmed by the NCIPlot analysis that shows a quite extended green isosurface located between the C–H bond and the π system.

Fourier transform infrared (FT-IR) spectroscopy

FT-IR spectroscopy was used as a complementary technique to study the interactions between the functional groups. Multicomponent material formation can be determined by shifting the wavenumber or changing the peak intensities of functional groups in comparison with their constituents.[47] Fig. 12 shows the FT-IR spectra of the ETZ and cocrystals. The significant bands of ETZ that are involved in the formation of cocrystals are at 1626 cm^{-1} due to the carbonyl stretching group (C=O) and the bands at 3165 and 3366

Table 3 Characteristic FT-IR bands of ETZ and their respective positions on the cocrystals

Compound	Wavenumber (cm^{-1})		
	C=O stretching	N–H asymmetric	N–H symmetric
ETZ	1626	3165	3366
ETZ–CAT	1585	3153	3425
ETZ–RES	1585	3181	3416
ETZ–HQ	1591	3148	3322
ETZ–PHL	1613	3171	3368

cm^{-1}, ascribed to the symmetric and asymmetric stretching modes of N–H, respectively. Shifts in the mentioned bands are clearly observed, indicating the formation of cocrystals, which is in good agreement with previous X-ray diffraction results. The relevant bands of ETZ and their respective shifts in the cocrystals are summarized in Table 3.

Thermal analysis

To assess the thermal stability of the cocrystals, their melting points and weight losses were analyzed using simultaneous differential scanning calorimetry (DSC) and thermogravimetric analysis (TGA). Fig. 13 shows DSC traces of the cocrystals. One major endothermic event was observed in each sample, which was ascribed to its melting point. While **ETZ–PHL** presented a melting point between those of the API and the coformer, a common behaviour already reported in pharmaceutical multicomponent materials,[48] the other cocrystals presented melting points below those of the parent components, thus indicating lower thermal stability. Interestingly, coformers with lower melting points (CAT and RES) led to the formation of cocrystals with lower melting points, indicating a positive correlation between the melting points of the coformer and those of the cocrystals. The melting points of the coformers and cocrystals are listed in Table 4.

No endothermic events are observed below the melting point, confirming the purity of the phases observed by PXRD. In addition, thermogravimetric analysis (TGA) demonstrated the integrity of the phases because no weight loss was observed below the melting point. The decomposition of the phases occurred only above the melting point, as can be
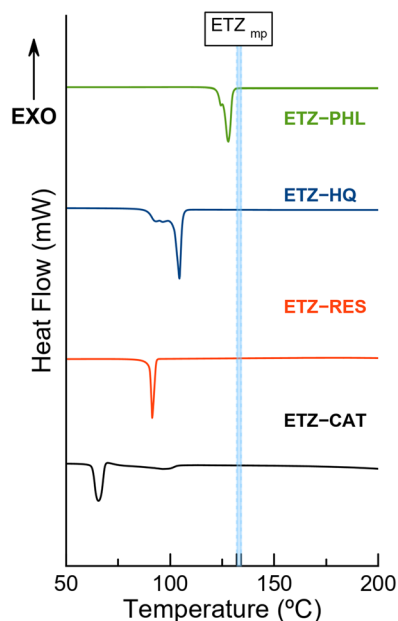

Fig. 13 Differential scanning calorimetry (DSC) traces of the pure cocrystals. Blue dotted lines correspond to a range of temperatures reported for the melting point of ETZ.

Table 4 Melting point of the components and cocrystals used in this work

Compound	Melting point (°C)	Cocrystal	Melting point (°C)
CAT	105	ETZ–CAT	65–66
RES	110	ETZ–RES	91.4
HQ	172	ETZ–HQ	103
PHL	116–117	ETZ–PHL	127
ETZ	132–134		

observed in Fig. S4.† In addition, DSC traces of novel cocrystals and isolated coformers with the corresponding onset and enthalpy values are given in Fig. S5 and S6,† respectively. Fig. 13 shows fusion–recrystallization–fusion events in the **ETZ–PHL** and **ETZ–HQ** samples, attributed to the transition among two/three non-identified phases, likely polymorph transformations. Surprisingly, despite the appearance of these phase transformations during the DSC experiment, the nature of such materials before and after the thermal experiment is identical, as supported by TGA results and confirmed by PXRD.

Stability studies

The stability of the cocrystals and their dissociation profiles were assessed in PBS buffer at 25 °C for 24 h (Fig. S7†).

Although no changes in color or texture were observed, PXRD revealed that none of the cocrystals was stable in aqueous medium. In fact, the cocrystals dissociated in less than 30 min. It should be noted that the stability study and dissolution profile of **ETZ–HQ** have been performed only as a matter of comparison in order to elucidate, if possible, a structure–property relationship. Thus, **ETZ–HQ** is not considered a suitable pharmaceutical cocrystal according to the FDA's restrictions on this polyphenol.

Low stability under accelerated aging conditions (40 °C and 75% RH) was also observed. The PXRD patterns of the samples after four months under the above-mentioned conditions demonstrated that only **ETZ–PHL** remained stable, whereas **ETZ–RES** and **ETZ–HQ** showed partial dissociation after one month. Finally, **ETZ–CAT** dissociated in the first 24 h and completely dissociated after one week (Fig. 14).

Powder dissolution profile

As observed in the previous section, cocrystals are not thermodynamically stable in aqueous solutions. Therefore, to monitor the evolution of ETZ concentration, the dissolution profile of pure ETZ and cocrystals was determined by UV-vis spectrophotometry in PBS buffer (pH 6.8), simulating the
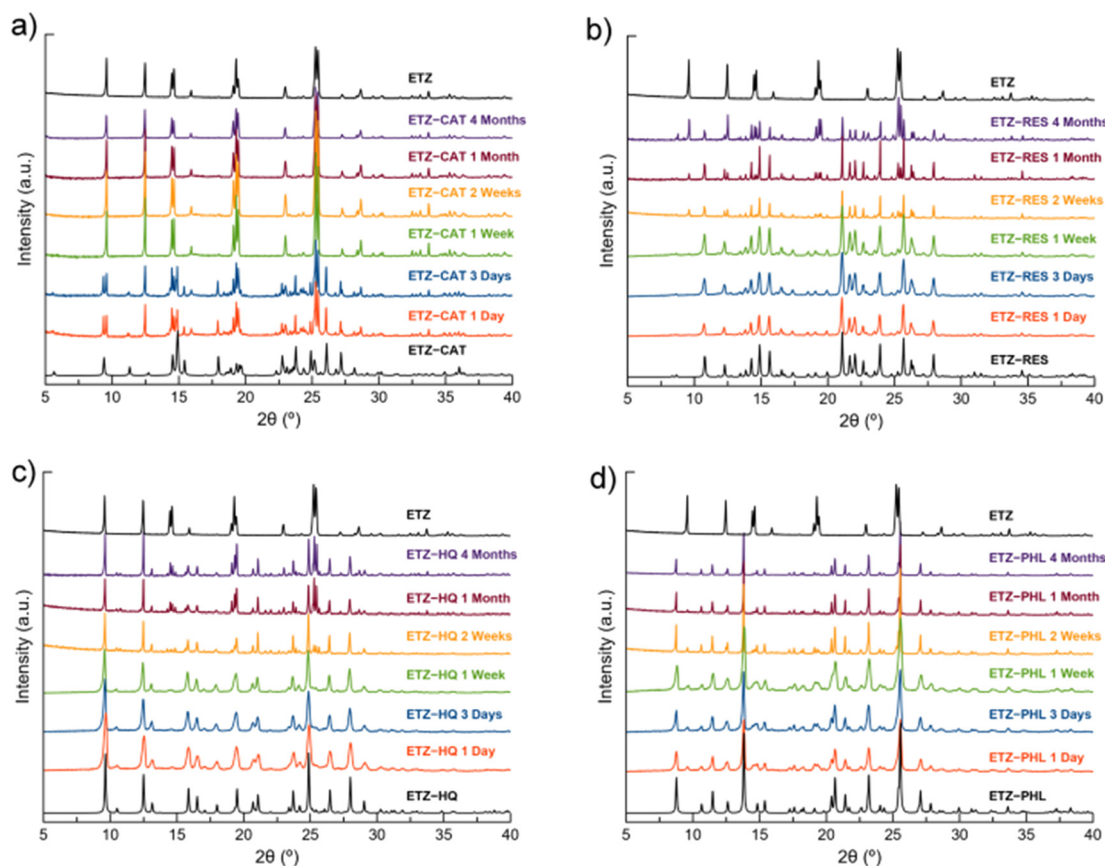
Fig. 14 PXRD patterns of **ETZ–CAT** (a), **ETZ–RES** (b), **ETZ–HQ** (c) and **ETZ–PHL** (d) with respect to the stability under accelerated aging conditions (40 °C, 75% RH) at different time intervals.
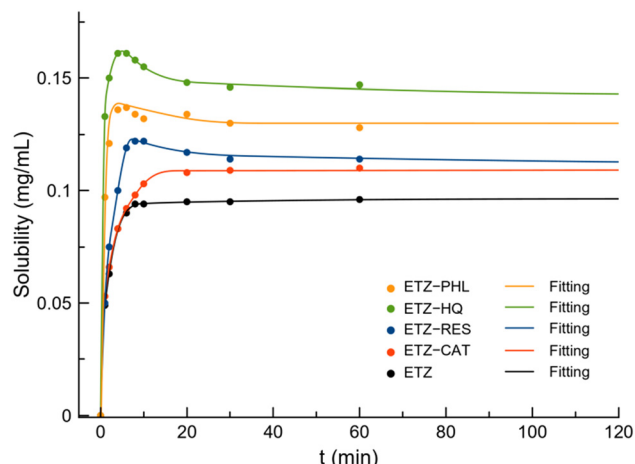
Fig. 15 Dissolution profile of ETZ and cocrystals at 120 min.

intestinal environment. Fig. 15 shows the dissolution profile of ETZ and cocrystals up to 120 min of experiments while Fig. S8† represents the complete dissolution profile up to 24 h. The solubility of ETZ is reported to be <0.05 mg mL^{-1} in PBS (pH 7.4) and increased up to 0.5 mg mL^{-1} in HCl aqueous solution at pH 1.2.[49,50] Fig. S9† shows the PXRD patterns of the reported ETZ cocrystals after powder dissolution experiments.

The equilibrium solubility of ETZ experimentally obtained in PBS (pH 6.8) is 0.09 mg mL^{-1}, which is in good agreement with the reported solubility, while the solubility obtained for the cocrystals increased in the order **ETZ–CAT** (0.111 mg mL^{-1}) < **ETZ–RES** (0.113 mg mL^{-1}) < **ETZ–PHL** (0.131 mg mL^{-1}) < **ETZ–HQ** (0.141 mg mL^{-1}). Interestingly, a "spring and parachute" effect was observed in all the cocrystals except **ETZ–CAT**. This effect is well known among multicomponent materials and allows supersaturation and fast liberation of the API at the initial stages of the dissolution process.[51]

Based on the position of the hydroxyl substituents of the polyphenolic coformers in the supramolecular arrangement, crystal structural analysis provides a plausible explanation for the observed solubility trend. **ETZ–HQ** cocrystals display ETZ dimer disruption in favor of coformer shielding of the amide group while achieving a higher ETZ concentration at a faster rate. On the other hand, **ETZ–PHL**, **ETZ–RES**, and **ETZ–CAT** cocrystals exhibited better apparent solubility than ETZ, reaching a higher ETZ concentration below 10 min and subsequently decreasing over the API itself owing to the effective distance separation of ETZ dimers in their corresponding crystal structures.

Experimental

Materials

ETZ, the coformers, and all solvents were commercially available from Sigma-Aldrich (purity >98%, Sigma-Aldrich, St. Louis, MO, USA) and were used as received.

General procedure for cocrystal synthesis

Mechanochemical synthesis was conducted by liquid-assisted grinding (LAG) in a Retsch MM2000 ball mill operating at 25 Hz frequency, using stainless steel jars along with two stainless steel balls of 7 mm diameter. All reaction syntheses lasted for 10 min, except for **ETZ–PHL** that lasted for 20 min. Reactions were repeated to ensure reproducibility.

ETZ–CAT was obtained by LAG of a mixture of ETZ (1 mmol, 165.18 mg) and the respective coformer (0.5 mmol, 55.05 mg), in a 2:1 stoichiometric ratio, using 100 μL of hexane as liquid additive.

ETZ–RES and **ETZ–HQ** were obtained by LAG of a mixture of ETZ (1 mmol, 165.18 mg) and the respective coformer (0.5 mmol, 55.05 mg), in a 2:1 stoichiometric ratio, using 100 μL of ethanol as liquid additive.

ETZ–PHL was obtained by LAG of a mixture of ETZ (1 mmol, 165.18 mg) and PHL (0.5 mmol, 63.076 mg), in a 2:1 stoichiometric ratio, using 100 μL of acetonitrile as liquid additive.

After milling, the bulk materials were collected and evaluated by PXRD to determine the formation of new materials.

Preparation of single crystals

Single crystals of the phases were grown by slow solvent evaporation at room temperature using saturated solutions of the polycrystalline material obtained from mechanical synthesis. Ethanol was used for preparing the saturated solutions of **ETZ–CAT**, **ETZ–RES**, and **ETZ–HQ**, and acetonitrile for **ETZ–PHL**. Suitable crystals for SCXRD appeared after 2 days of slow solvent evaporation at room temperature.

X-ray diffraction analysis

Measured crystals were prepared under inert conditions and immersed in perfluoropolyether as protecting oil for manipulation. Suitable crystals were mounted on MiTeGen Micromounts™, and these samples were used for data collection. Data were collected at 298 K on a Bruker D8 Venture diffractometer (Bruker-AXS, Karlsruhe, Germany) with graphite-monochromated CuKα radiation (λ = 1.54178 Å). Integration and scaling of the intensity data were accomplished using the APEX4 suite.[52] The structures were solved by intrinsic phasing using the ShelXT program,[53] which revealed the position of all non-hydrogen atoms. These atoms were refined on F^2 by a full-matrix least-squares procedure using the anisotropic displacement parameter.[54] All hydrogen atoms were located in difference Fourier maps and included as fixed contributions riding on attached atoms with isotropic thermal displacement parameters 1.2 or 1.5 times those of the respective atom. The Olex2 (ref. 55) software was used as a graphical interface. Intermolecular interactions were calculated using the PLATON program.[56] Molecular graphics were generated using Olex2 (ref. 55) and Mercury software.[57] The crystallographic data for the reported

Table 5 Crystal data and refinement details of ETZ cocrystals

	ETZ–CAT	ETZ–RES	ETZ–HQ	ETZ–PHL
Formula	$C_{24}H_{28}N_2O_6$	$C_{24}H_{28}N_2O_6$	$C_{12}H_{14}NO_3$	$C_{24}H_{28}N_2O_7$
Formula weight	440.48	440.48	220.24	456.48
Crystal system	Triclinic	Monoclinic	Triclinic	Monoclinic
Space group	$P\bar{1}$	$P2_1/c$	$P\bar{1}$	Pn
a (Å)	7.7814(12)	10.2189(6)	7.2548(5)	9.9310(7)
b (Å)	10.0144(12)	13.8655(10)	9.0844(6)	10.0681(6)
c (Å)	15.979(2)	16.3778(10)	9.5457(5)	12.1027(8)
α (°)	87.193(7)	90	99.864(3)	90
β (°)	77.808(7)	93.473(3)	99.082(3)	99.780(4)
γ (°)	69.864(7)	90	107.888(3)	90
Volume (Å³)	1142.3(3)	2316.3(3)	574.80(6)	1192.52(14)
Z	2	4	2	2
d_{calc} (g cm⁻³)	1.281	1.263	1.273	1.271
$F(000)$	468	936	234	484
Total reflections	12 456	31 842	9342	16 420
Unique reflections	3966 [R(int) = 0.0261]	4058 [R(int) = 0.0538]	1958 [R(int) = 0.0641]	3793 [R(int) = 0.0556]
Completeness (%)	98	99	97	99
Data/restraints/parameters	3966/0/293	4058/0/294	1958/0/148	3793/2/304
Goodness of fit on F^2	1.043	1.065	1.065	1.040
R_1,[a] wR_2[b] [$I > 2\sigma(I)$]	0.0593, 0.1876	0.0395, 0.1139	0.0443, 0.1235	0.0404, 0.1043
R_1,[a] wR_2[b] [$I > 2\sigma(I)$] (all data)	0.0686, 0.1971	0.0447, 0.1208	0.0465, 0.1264	0.0472, 0.1108
CCDC number	2247944	2247945	2247946	2247947

[a] $R_1 = \sum||F_o| - |F_c||/\sum|F_o|.$ [b] $wR_2 = \sum w(|F_o|^2 - |F_c|^2)^2/\sum w(|F_o|^2)^{1/2}.$

structures were deposited with the Cambridge Crystallographic Data Center as supplementary publication no. CCDC 2247944–2247947. Additional crystal data are shown in Table 5.

Powder X-ray diffraction (PXRD) analysis was performed at room temperature on a Bruker D8 Advance Vario diffractometer (Bruker-AXS, Karlsruhe, Germany) equipped with a LYNXEYE detector and CuKα$_1$ radiation (1.5406 Å). The diffractograms were collected over an angular range of 5–40° (2θ) with a step size of 0.02° (2θ) and a constant counting time of 5 s per step.

Theoretical studies

The energies reported herein were computed either using Gaussian-16 (ref. 58) at the PBE0 (ref. 59)-D3 (ref. 60)/def2-TZVP[61]) level of theory using the supramolecular approach for the π-stacking dimers or using the quantum theory of "atoms-in-molecules"[62] at the same level by means of the AIMAll program[63] for the H-bonding networks. For the former the BSSE correction[64] has been applied, and for the latter we have used the kinetic energy density values at the bond critical points that emerge upon complexation and applying the methodology proposed by Espinosa et al.[46] This methodology has been recently used by some of us to evaluate noncovalent interactions in the solid state.[65–72] The NCIPlot isosurfaces[73,74] have been generated using the AIMAll program[63] with the PBE0-D3/def2-TZVP wavefunction. The MEP surface plots have been performed using the 0.001 a.u. isosurface as the best estimate of the van der Waals envelope.

Fourier transform infrared (FT-IR) spectroscopy

Fourier transform infrared (FTIR) spectroscopy measurements were performed on a Bruker Tensor 27 FT-IR instrument (Bruker Corporation, Billerica, MA, USA) equipped with a single-reflection diamond crystal platinum ATR unit and an OPUS data collection program. The scanning range was 4000–400 cm⁻¹ with a resolution of 4 cm⁻¹.

Thermal analysis

Simultaneous differential scanning calorimetry (DSC) and thermogravimetric analysis were performed using a Mettler Toledo TGA/DSC1 thermal analyzer (Mettler Toledo, Columbus, OH, USA). Samples (3–5 mg) were placed into sealed aluminum pans and heated in a stream of nitrogen (100 mL min⁻¹) from 25 to 400 °C at a heating rate of 10 °C min⁻¹. Additional measurements were carried out using a Mettler-Toledo DSC-822e calorimeter. The calorimeter was calibrated with indium of 99.99% purity (m.p.: 156.4 °C; ΔH: 28.14 J g⁻¹).

Stability studies

The stability of ETZ and cocrystals in aqueous solution was evaluated through slurry experiments in which an excess of the pure samples was added to 10 mL of phosphate buffer (pH 6.8) and stirred for 24 h at 25 °C in sealed vials. The solids were collected at different times, filtered, dried at 35 °C and further analyzed by PXRD. The stability was also assessed at accelerated aging conditions (40 °C and 75% RH) by placing powder samples in a Memmert HPP110 climate chamber (Memmert, Schwabach, Germany) up to 2 months. The samples were analyzed by PXRD periodically to evaluate

possible phase transformation during the time of the experiment.

Powder dissolution profile

Powder dissolution profile studies for pure ETZ and for each new phase were performed using a Varian Cary 50 ultraviolet (UV)-visible spectrophotometer (Agilent Technologies, Santa Clara, CA, USA). The calibration curve was prepared using standard solutions of ETZ, which were analyzed at 244 nm to avoid coformer interference. Samples for the solubility studies were prepared following the shake-flask method. Saturated solutions of each solid were prepared by adding excess solid to a PBS buffer solution at pH 6.8. The solutions were stirred for 24 h at 25 °C in a water bath until thermodynamic equilibrium was reached. During this time, aliquots of the solutions at different times were taken, filtered through 0.22 μm polyether sulfone (PES) filters and directly measured by UV-vis spectrophotometry. Appropriate dilutions were made to obtain measurable absorbance values. The absorbance measurements were thereafter used to quantify the ETZ solubilized in each sample. The remaining solids were analyzed by PXRD to identify the crystalline phases and thus to check the stability of the initial crystalline phase.

Conclusions

Rational screening of the synthon preference of ethenzamide revealed the suitability of polyphenolic ligands as coformers. As expected, the amide–carboxylic supramolecular heterosynthon dominates the molecular recognition pattern between ETZ and polyphenolic coformers. Interestingly, reciprocal N–H⋯O bonds build self-assembled ETZ dimers in the **ETZ–CAT**, **ETZ–RES** and **ETZ–PHL** cocrystals. This ETZ amide:amide $R_2^2(8)$ homosynthon has also been described in the crystal structure of pure ethenzamide and is preserved in the referred cocrystals although with larger distances due to the introduction of the corresponding coformers. Conversely, such a recognition pattern is disrupted in the crystal structure of **ETZ–HQ**, in which the presence of two close HQ ligands prevents the formation of such reciprocal amide:amide H-bonds, leading to an $R_1^2(6)$ synthon instead. The construction of the different architectures is supported by the calculated energy values, with the energy associated to the $R_1^2(6)$ synthon (−9.35 kcal mol^{-1}) being larger than those of $R_2^2(8)$ synthons within the ETZ dimers (**ETZ–RES** −6.43 kcal mol^{-1} < **E TZ–CAT** −7.06 kcal mol^{-1} < **ETZ–PHL** −8.10 kcal mol^{-1}).

Theoretical studies further evaluate the strength of all intermolecular interactions, with the total H-bonding energy being **ETZ–HQ** (−12.20 kcal mol^{-1}) < **ETZ–RES** (−25.76 kcal mol^{-1}) < **ETZ–CAT** (−28.18 kcal mol^{-1}) < **ETZ–PHL** (−34.71 kcal mol^{-1}). In addition, different π–π stacking modes were observed, which are in agreement with the experimental data in the solid state of the novel cocrystals. Remarkably, some structure–property relationships can be explained according to the overall energy values of the reported structures. For

instance, the solubility of the novel multicomponent phases was enhanced compared to that of ETZ alone according to the following order: **ETZ–CAT** (×1.2) < **ETZ–RES** (×1.3) < **ETZ–PHL** (×1.5) < **ETZ–HQ** (×1.6). Note that the weaker structure (**ETZ–HQ**) shows the higher apparent solubility simply because it is easier to dissociate/hydrate. Their dissolution profiles also showed an interesting "spring and parachute" profile, which might be of interest for immediate-release formulations. Unfortunately, the novel pharmaceutical cocrystals do not show significant improvement regarding either the thermal or the thermodynamic stability when compared to the parent components. For instance, all ETZ cocrystals underwent dissociation under simulated physiological conditions before 24 h. Although the different disposition of the hydroxyl groups in the isomeric polyphenolic coformers determines the observed differences in the physicochemical behaviour of the novel cocrystals, the overall similarity of their crystal architectures resulted in similar weaknesses for all new drug formulations. These latter results compromise the development of future studies on these pharmaceutical cocrystals.

Author contributions

D. C.-L. conceived the project. F. J. A.-M., C. A.-P., A. I. and A. D.-M. performed the synthesis and characterization of the studied compounds. D. C.-L. solved the crystal structures. A. F. performed the theoretical calculations. D. C.-L. analyzed the data. D. C.-L., F. J. A.-M and A. D.-M. wrote the paper. D. C.-L. supervised the project. D. C.-L. and A. D.-M. were responsible for funding acquisition.

Conflicts of interest

There are no conflicts to declare.

References

1 O. Kawano, T. Sawabe, N. Misaki and K. Fukawa, *Jpn. J. Pharmacol.*, 1978, **28**, 829–835.
2 H. Uehara, H. Otsuka and K. Izumi, *Cancer Lett.*, 1998, **135**, 83–90.
3 S. Aoki, T. Mizutani and K. Danjo, *Chem. Pharm. Bull.*, 2000, **48**, 140–141.
4 S. Aitipamula, P. S. Chow and R. B. H. Tan, *CrystEngComm*, 2009, **11**, 1823–1827.
5 M. Kazuhiro, N. Yoshinobu, Y. Etsuo, O. Toshio and Y. Keiji, *Int. J. Pharm.*, 1994, **108**, 167–172.

6   K. Danjo, T. Nakata and A. Otsuka, *Chem. Pharm. Bull.*, 1997, **45**, 1840–1844.

7   M. Ozawa, K. Hasegawa, Y. Yonezawa and H. Sunada, *Chem. Pharm. Bull.*, 2002, **50**, 802–807.

8   B. Saikia, P. Bora, R. Khatioda and B. Sarma, *Cryst. Growth Des.*, 2015, **15**, 5593–5603.

9   R. Kumar Bandaru, S. R. Rout, G. Kenguva, B. Gorain, N. A. Alhakamy, P. Kesharwani and R. Dandela, *Front. Pharmacol.*, 2021, **12**, 2954.

10 *Generally Recognized as Safe (GRAS)|FDA*, **https://www.fda. gov/food/food-ingredients-packaging/generally-recognized-safe-gras**, (accessed 2 March 2023).

11 *Substances Added to Food (formerly EAFUS)|FDA*, **https://www. fda.gov/food/food-additives-petitions/substances-added-food-formerly-eafus**, (accessed 2 March 2023).

12 S. Aitipamula, A. B. H. Wong, P. S. Chow and R. B. H. Tan, *CrystEngComm*, 2012, **14**, 8515–8524.

13 V. M. Hariprasad, S. K. Nechipadappu and D. R. Trivedi, *Cryst. Growth Des.*, 2016, **16**, 4473–4481.

14 R. Khatioda, B. Saikia, P. J. Das and B. Sarma, *CrystEngComm*, 2017, **19**, 6992–7000.

15 A. Kozak, P. H. Marek and E. Pindelska, *J. Pharm. Sci.*, 2019, **108**, 1476–1485.

16 S. Aitipamula, P. S. Chow and R. B. H. Tan, *CrystEngComm*, 2009, **11**, 889–895.

17 S. Aitipamula, P. S. Chow and R. B. H. Tan, *Cryst. Growth Des.*, 2010, **10**, 2229–2238.

18 S. Aitipamula, P. S. Chow and R. B. H. Tan, *CrystEngComm*, 2010, **12**, 3691–3697.

19 G. Pekoe, K. van Dyke, D. Peden, H. Mengoli and D. English, *Agents Actions*, 1982, **12**, 371–376.

20 M. Wan, J. Fang, J. Xue, J. Liu, J. Qin, Z. Hong, J. Li and Y. Du, *Int. J. Mol. Sci.*, 2022, **23**, 8550.

21 A. Scalbert, I. T. Johnson and M. Saltmarsh, *Am. J. Clin. Nutr.*, 2005, **81**, S215–S217.

22 S. Quideau, D. Deffieux, C. Douat-Casassus and L. Pouységu, *Angew. Chem., Int. Ed. Engl.*, 2011, **50**, 586–621.

23 M. Abbas, F. Saeed, F. M. Anjum, M. Afzaal, T. Tufail, M. S. Bashir, A. Ishtiaq, S. Hussain and H. A. R. Suleria, *Int. J. Food Prop.*, 2017, **20**, 1689–1699.

24 N. Magaña-Vergara, P. de la Cruz-Cruz, A. Peraza-Campos, F. Martínez-Martínez and J. González-González, *Crystals*, 2018, **8**, 130.

25 J. S. González-González, A. M. M. Martínez-Santiago, F. J. Martínez-Martínez, M. J. Emparán-Legaspi, A. Pineda-Contreras, M. Flores-Alamo and H. García-Ortega, *Crystals*, 2020, **10**, 569.

26 Y. Xiao, L. Zhou, H. Hao, Y. Bao, Q. Yin and C. Xie, *Cryst. Growth Des.*, 2021, **21**, 1202–1217.

27 C. Verdugo-Escamilla, C. Alarcón-Payer, F. J. Acebedo-Martínez, R. Fernández-Penas, A. Domínguez-Martín and D. Choquesillo-Lazarte, *Crystals*, 2022, **12**, 798.

28 F. H. Allen, *Acta Crystallogr., Sect. B: Struct. Sci.*, 2002, **58**, 380–388.

29 F. Acebedo-Martínez, C. Alarcón-Payer, L. Rodríguez-Domingo, A. Domínguez-Martín, J. Gómez-Morales and D. Choquesillo-Lazarte, *Crystals*, 2021, **11**, 1339.

30 S. K. Nechipadappu and D. R. Trivedi, *J. Mol. Struct.*, 2018, **1171**, 898–905.

31 S. K. Nechipadappu, V. Tekuri and D. R. Trivedi, *J. Pharm. Sci.*, 2017, **106**, 1384–1390.

32 K. R. Back, R. J. Davey, T. Grecu, C. A. Hunter and L. S. Taylor, *Cryst. Growth Des.*, 2012, **12**, 6110–6117.

33 R. Khatioda, P. Bora and B. Sarma, *Cryst. Growth Des.*, 2018, **18**, 4637–4645.

34 K. Moribe, M. Tsuchiya, Y. Tozuka, K. Yamaguchi, T. Oguchi and K. Yamamoto, *Chem. Pharm. Bull.*, 2004, **52**, 524–529.

35 V. M. Hariprasad, S. K. Nechipadappu and D. R. Trivedi, *Cryst. Growth Des.*, 2016, **16**, 4473–4481.

36 S. Aitipamula, P. S. Chow and R. B. H. Tan, *Cryst. Growth Des.*, 2010, **10**, 2229–2238.

37 J. Li, C. Li, X. Ji, Q. Sun, Z. Li, H. Liu, L. Zhou, D. Jing, J. Gong and W. Chen, *New J. Chem.*, 2022, **46**, 8708–8719.

38 S. Aitipamula, P. S. Chow and R. B. H. Tan, *Acta Crystallogr., Sect. E: Struct. Rep. Online*, 2010, **66**, o1045–o1046.

39 K. K. Sarmah, K. Boro, M. Arhangelskis and R. Thakuria, *CrystEngComm*, 2017, **19**, 826–833.

40 R. Khatioda, B. Saikia, P. J. Das and B. Sarma, *CrystEngComm*, 2017, **19**, 6992–7000.

41 J. Potticary, C. Hall, V. Hamilton, J. F. McCabe and S. R. Hall, *Cryst. Growth Des.*, 2020, **20**, 2877–2884.

42 S. Pagola and P. W. Stephens, *Acta Crystallogr., Sect. C: Cryst. Struct. Commun.*, 2009, **65**, o583–o586.

43 C. Loschen and A. Klamt, *J. Pharm. Pharmacol.*, 2015, **67**, 803–811.

44 Y. A. Abramov, C. Loschen and A. Klamt, *J. Pharm. Sci.*, 2012, **101**, 3687–3697.

45 D. Braga, L. Maini and F. Grepioni, *Chem. Soc. Rev.*, 2013, **42**, 7638.

46 E. Espinosa, E. Molins and C. Lecomte, *Chem. Phys. Lett.*, 1998, **285**, 170–173.

47 A. Heinz, C. J. Strachan, K. C. Gordon and T. Rades, *J. Pharm. Pharmacol.*, 2009, **61**, 971–988.

48 G. Perlovich, *Acta Crystallogr., Sect. B: Struct. Sci., Cryst. Eng. Mater.*, 2020, **76**, 696–706.

49 R. Khatioda, B. Saikia, P. J. Das and B. Sarma, *CrystEngComm*, 2017, **19**, 6992–7000.

50 R. Khatioda, P. Bora and B. Sarma, *Cryst. Growth Des.*, 2018, **18**, 4637–4645.

51 D. D. Bavishi and C. H. Borkhataria, *Prog. Cryst. Growth Charact. Mater.*, 2016, **62**, 1–8.

52 Bruker, *APEX3*, 2022.

53 G. M. Sheldrick, *Acta Crystallogr., Sect. A: Found. Adv.*, 2015, **71**, 3–8.

54 G. M. Sheldrick, *Acta Crystallogr., Sect. C: Struct. Chem.*, 2015, **71**, 3–8.

55 O. v. Dolomanov, L. J. Bourhis, R. J. Gildea, J. A. K. Howard and H. Puschmann, *J. Appl. Crystallogr.*, 2009, **42**, 339–341.

56 A. L. Spek, *Acta Crystallogr., Sect. D: Biol. Crystallogr.*, 2009, **65**, 148–155.

57 C. F. Macrae, I. Sovago, S. J. Cottrell, P. T. A. Galek, P. McCabe, E. Pidcock, M. Platings, G. P. Shields, J. S. Stevens,

M. Towler and P. A. Wood, *J. Appl. Crystallogr.*, 2020, **53**, 226–235.

58 M. J. Frisch, G. W. Trucks, H. B. Schlegel, G. E. Scuseria, M. A. Robb, J. R. Cheeseman, G. Scalmani, V. Barone, B. Mennucci, G. A. Petersson, H. Nakatsuji, M. Caricato, X. Li, H. P. Hratchian, A. F. Izmaylov, J. Bloino, G. Zheng, J. L. Sonnenberg, M. Hada, M. Ehara, K. Toyota, R. Fukuda, J. Hasegawa, M. Ishida, T. Nakajima, Y. Honda, O. Kitao, H. Nakai, T. Vreven, J. A. Montgomery Jr., J. E. Peralta, F. Ogliaro, M. Bearpark, J. J. Heyd, E. Brothers, K. N. Kudin, V. N. Staroverov, R. Kobayashi, J. Normand, K. Raghavachari, A. Rendell, J. C. Burant, S. S. Iyengar, J. Tomasi, M. Cossi, N. Rega, J. M. Millam, M. Klene, J. E. Knox, J. B. Cross, V. Bakken, C. Adamo, J. Jaramillo, R. Gomperts, R. E. Stratmann, O. Yazyev, A. J. Austin, R. Cammi, C. Pomelli, J. W. Ochterski, R. L. Martin, K. Morokuma, V. G. Zakrzewski, G. A. Voth, P. Salvador, J. J. Dannenberg, S. Dapprich, A. D. Daniels, O. Farkas, J. B. Foresman, J. v. Ortiz, J. Cioslowski and D. J. Fox, *Gaussian16 (Revision A.03)*, 2016.

59 J. P. Perdew, K. Burke and M. Ernzerhof, *Phys. Rev. Lett.*, 1996, **77**, 3865–3868.

60 S. Grimme, J. Antony, S. Ehrlich and H. Krieg, *J. Chem. Phys.*, 2010, **132**, 154104.

61 F. Weigend and R. Ahlrichs, *Phys. Chem. Chem. Phys.*, 2005, **7**, 3297.

62 R. F. W. Bader, *Chem. Rev.*, 1991, **91**, 893–928.

63 T. A. Keith, *AIMALL (Version 19.10.12)*, TK Gristmill Software, Overland Park, KS, USA, 2019.

64 S. F. Boys and F. Bernardi, *Mol. Phys.*, 1970, **19**, 553–566.

65 Z. M. Efimenko, A. A. Eliseeva, D. M. Ivanov, B. Galmés, A. Frontera, N. A. Bokach and V. Yu. Kukushkin, *Cryst. Growth Des.*, 2021, **21**, 588–596.

66 L. E. Zelenkov, D. M. Ivanov, E. K. Sadykov, N. A. Bokach, B. Galmés, A. Frontera and V. Yu. Kukushkin, *Cryst. Growth Des.*, 2020, **20**, 6956–6965.

67 N. S. Soldatova, P. S. Postnikov, V. v. Suslonov, T. Yu. Kissler, D. M. Ivanov, M. S. Yusubov, B. Galmés, A. Frontera and V. Yu. Kukushkin, *Org. Chem. Front.*, 2020, **7**, 2230–2242.

68 E. A. Katlenok, M. Haukka, O. V. Levin, A. Frontera and V. Yu. Kukushkin, *Chem. – Eur. J.*, 2020, **26**, 7692–7701.

69 A. v. Rozhkov, A. A. Eliseeva, S. v. Baykov, B. Galmés, A. Frontera and V. Yu. Kukushkin, *Cryst. Growth Des.*, 2020, **20**, 5908–5921.

70 A. v. Rozhkov, I. v. Ananyev, R. M. Gomila, A. Frontera and V. Yu. Kukushkin, *Inorg. Chem.*, 2020, **59**, 9308–9314.

71 C. Verdugo-Escamilla, C. Alarcón-Payer, A. Frontera, F. J. Acebedo-Martínez, A. Domínguez-Martín, J. Gómez-Morales and D. Choquesillo-Lazarte, *Crystals*, 2020, **10**, 1088.

72 R. Barbas, V. Kumar, O. Vallcorba, R. Prohens and A. Frontera, *Crystals*, 2020, **10**, 1126.

73 E. R. Johnson, S. Keinan, P. Mori-Sánchez, J. Contreras-García, A. J. Cohen and W. Yang, *J. Am. Chem. Soc.*, 2010, **132**, 6498–6506.

74 J. Contreras-García, E. R. Johnson, S. Keinan, R. Chaudret, J.-P. Piquemal, D. N. Beratan and W. Yang, *J. Chem. Theory Comput.*, 2011, **7**, 625–632.